Measuring the cross section of the ^{15}N(α,γ)^{19}F reaction using a single-fluid bubble chamber. (Draft v9.4)

D. Neto and C. Ugalde*
Department of Physics, University of Illinois at Chicago, Chicago, Illinois 60607, USA

B. DiGiovine† and K. Bailey, T. O'Connor, K. E. Rehm, S. Riordan, R. Talwar
Physics Division, Argonne National Laboratory, Argonne, Illinois 60439, USA

J. F. Benesch, B. Cade, J. M. Grames, A. Hofler, R. Kazimi,
D. Meekins, M. McCaughan, D. Moser, M. Poelker, R. Suleiman
Thomas Jefferson National Accelerator Facility, Newport News, Virginia 23606, USA

R. Holt
Kellogg Radiation Laboratory, Caltech, Pasadena, California 91125, USA
(Dated: August 3, 2022)

^{15}N(α,γ)^{19}F is believed to be the primary means of nucleosynthesis of Fluorine in AGB and WR stars. In this paper, we present the use of a single-fluid bubble chamber to measure the time-inverse photo-dissociation reaction. Benefiting from increases of the luminosity, over methods using thin-films or gas targets, by several orders of magnitude from both the factor of 10-100 gain from the reciprocity theorem and the use of a thicker liquid target. We will discuss the results of test measurements at Jefferson National Lab, measuring the cross section of the photodisintegration process ^{19}F(γ, α)^{15}N by bombarding a superheated fluid of C_3F_8 with bremsstrahlung γ-rays. Simulating the γ-ray beam in GEANT4 and convoluting the γ-ray spectrum with the Breit-Wigner cross section. Using this technique, we measure cross sections of the time-reversed ^{15}N(α,γ)^{19}F reaction down to the range of $\sim$ 80 picobarns. We also discuss future changes to the experimental setup, potentially pushing measurements down to the single picobarn range.

I. INTRODUCTION

Radiative capture reactions are of fundamental importance in astrophysics. Protons, neutrons and α particles are abundant in many stellar environments and can interact through (n,γ), (p,γ) and (α, γ) reactions with heavier nuclei under hydrostatic or explosive conditions or in the Big Bang. Reactions involving α particles usually have the lowest cross sections as the higher Coulomb barrier between the nuclei slows down these capture processes. In most cases the cross sections are so small that it is difficult to measure these reactions at stellar conditions in the laboratory using current technologies. For two of the important astrophysical reactions, ^{2}H(α,γ)^{6}Li [1] and ^{12}C(α,γ)^{16}O [2], the measured cross sections are in the range of tens of picobarn, thus, requiring a low-background environment and long running times.

Most experiments measure the radiative capture cross sections either in direct kinematics (i.e. a light ion beam on a heavy target) or in inverse kinematics (a heavy ion beam on a light target) usually detecting the γ-rays in the exit channel. More recent techniques detect the recoiling heavy ion [3, 4] and in more complex experimental setups both the γ-ray and the recoil in coincidence [5]. Ubiquitous beam and target contamination and contributions from cosmic rays are usually the main sources of background that limit the sensitivity of these measurements. Furthermore the low density of the targets ($\sim$1-10 μg/cm^2) prolongs the time needed to measure the cross sections, thus increasing the contributions from cosmic rays and other environmental backgrounds as well.

One possible method for improving the statistics of these measurements is to take advantage of the time-reversal symmetry of nuclear reactions that involve strong and electromagnetic interactions and measure the photodisintegration of nuclei into a light ion (proton, neutron, or α particle) and a heavier residual nucleus. Because of phase space transformations, photodisintegration reactions can have cross sections which are several orders of magnitude higher than the corresponding radiative capture process [6, 7]. Since the underlying matrix elements are identical for both processes, they can be determined by either approach.

The method described in this paper employs the advantages of the time-reverse reaction mentioned above using a thick ($\sim$1-10 g/cm^2) liquid target and a γ-ray beam. It can be adapted for measuring some of the most important nuclear reactions in stellar environments. The luminosity of this technique is orders of magnitude higher than that of some of the best direct measurements performed to date using existing γ-ray facilities.

In the experiments discussed below, the residual particles from the photodisintegration are detected with a bubble chamber [8]. The prime example of a radiative capture process that can be studied with the photodisso-

* cugalde@uic.edu
† Current address: Los Alamos National Laboratory.

ciation technique is the $^{12}C(\alpha,\gamma)^{16}O$ reaction using an oxygen containing liquid such as N_2O. While this reaction is key for understanding the nucleosynthesis in the universe, it has the complication that oxygen is not a monoisotopic element and, thus, requires the use of highly enriched ^{16}O compounds.

In a series of experiments we have therefore first studied the photodisintegration reaction $^{19}F(\gamma,\alpha)^{15}N$. Since ^{19}F is a monoisotopic element, no background reactions from the photodisintegration of other isotopes can occur. Furthermore since fluorine containing compounds (e.g. CH_2FCF_3, C_4F_{10} or C_3F_8) are used in Dark Matter experiments [9–11] sufficient information about these liquids in bubble chambers is available in the literature. Due to the fact that in the $^{15}N(\alpha,\gamma)^{19}F$ reaction excited states in ^{19}F are populated as well no direct comparison between the measured radiative capture and photodissociation yields can be made. However, sufficient information about energies, widths and branching ratios of the critical states in ^{19}F is available to calculate the expected yields for the $^{19}F(\gamma,\alpha)^{15}N$ reaction [12–14].

The first set of experiments were performed using a tunable γ-ray beam from the HIγS facility at Duke University [15] produced via inverse Compton scattering of laser light produced by electrons circulating in a storage ring [7, 8]. In these first experiments a good agreement between direct (α, γ) measurements and the time-inverse (γ, α) experiments was observed [7] covering the cross section range from 10 μb to about 3 nb. The lower cross section limit caused by background reactions between electrons and residual gas atoms in the storage ring [8].

In this paper we describe an extension of these measurements towards lower energies and smaller cross sections using a bremsstrahlung beam from the electron injector at Jefferson Lab.

II. SINGLE FLUID BUBBLE CHAMBER

Bubble chambers were invented more than 60 years ago[16] and have been used as detectors for high-energy physics experiments worldwide. During the last decade, they found a new application as continuously operating superheated detectors in the direct search of cold dark matter (CDM) [17–20]. While the original bubble chambers for high-energy experiments are kept in a superheated state for a very short time ($\sim$ 1 ms), the dark matter bubble chambers need to be active for extended time periods (hours to days). This introduces technical difficulties, as there are several processes that can induce bubble nucleation while the detector is waiting for a signal event. Unwanted bubble nucleation can be avoided by removing the compression piston and the buffer fluid or by using a buffer fluid that is in direct contact with the superheated fluid. The main difficulty using both, an active and a buffer fluid in a bubble chamber system, originates from chemical reactions and the solubility between

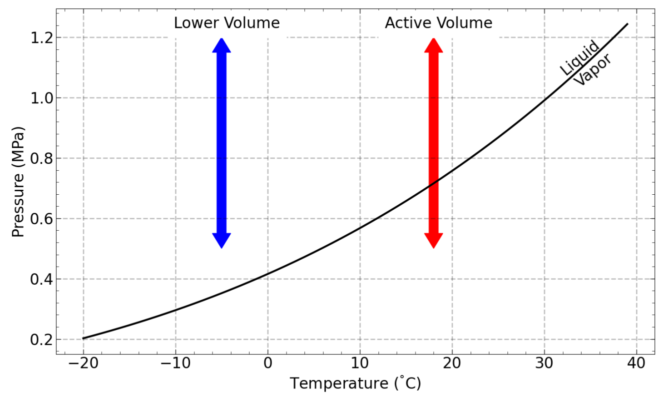

FIG. 1. (Color online) Phase diagram (pressure vs temperature) of C_3F_8. The red line shows the region covered in the fiducial region bombarded by the bremsstrahlung beam. This line crosses the phase boundary and creates a superheated liquid which can lead to bubble formation. The blue line represents a cooler region of the glass vessel. Being at a lower temperature, the liquid does not cross the phase boundary and therefore, does not lead to bubble formation.

the active target and the buffer fluid. This can produce solid residues that can be the source of unwanted nucleation. For this reason, these two-fluid bubble chambers are sometimes referred to as "dirty" chambers [21].

In this experiment we use a vertical vessel filled with C_3F_8. With a temperature gradient along the fluid. The lower part of the vessel is kept above the critical temperature and is, thus, not superheated. This prevents bubble nucleation in the crevices around the area where the hydraulic pressure control system and the fluid are in contact with each other.

Single fluid (or "clean") bubble chambers have first been used for the detection of long-lived, low-activity radio-isotopes (^{14}C, U or T) using diethyl ether or propane [21–23]. The bubble chamber used here employs the same principle.

The operational principle of a single-fluid bubble chamber can be seen in Fig. 1, which shows the phase diagram of C_3F_8 [24]. At a temperature of $> 18^oC$ and a pressure of 2 MPa, C_3F_8 is in its liquid form. Lowering the pressure to 0.5 MPa (red line in Fig. 1) brings the liquid into a superheated state which, since the products of a photodisintegration reaction deposit energy in the liquid, leads to the formation of a bubble [25]. At a temperature of -5^oC (blue line in Fig. 1) and pressures > 0.5 MPa, this region of the liquid does not cross the liquid-vapor barrier and, thus, will not result in superheating of the fluid.

A schematic of the single-fluid chamber is shown in Fig. 2. A small cylindrical glass vessel (diameter 3.6 cm) with a long neck (marked in blue) and filled with C_3F_8 (T=18°C, p=0.58 Mpa) is located in a box-shaped high-pressure vessel. The glass vessel is surrounded by mineral oil. The pressure in the high-pressure vessel can be adjusted to control the amount of superheat in the

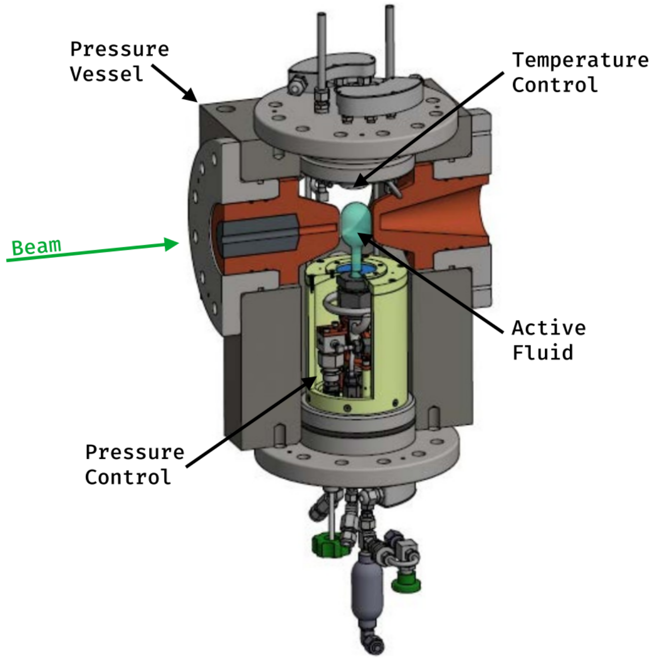

FIG. 2. (Color online) Schematic of the bubble chamber used in the experiment. The γ-ray beam impinges on the detector from the left. The C_3F_8 is located in a glass vessel with a long neck that extends down to the region of the hydraulic pressure control system. The temperature is regulated by a fluid that surrounds the glass vessel. There is a temperature gradient between the upper region of the glass vessel and the lower region around the glass stem. See text for details.

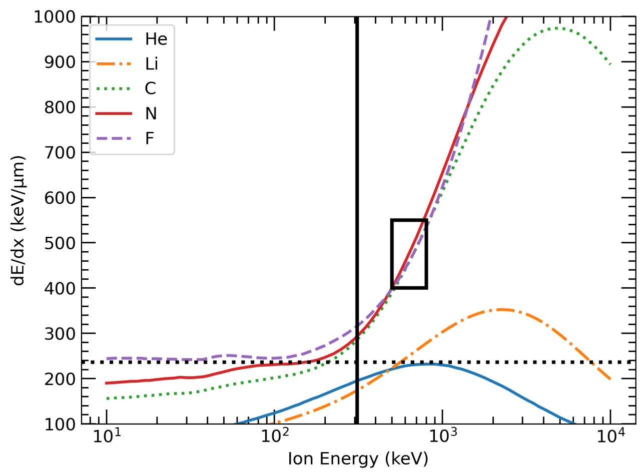

FIG. 3. (Color online) Stopping power vs. energy of various ion species moving in the C_3F_8 superheated liquid. The formation of a proto-bubble that will grow into an macroscopic (observable) bubble will depend on the amount of superheat in the liquid. The detector becomes active as pressure drops. An ion moving into the superheated liquid needs to fulfill two conditions to form a macroscopic bubble: the first condition is to be able to deposit enough energy into the active liquid. The dotted horizontal line represents a model [26] for the minimum stopping power (energy deposition) necessary to induce the formation of an observable bubble. The second condition requires the ion to have enough kinetic energy to form a macroscopic bubble. The vertical solid line is the critical kinetic energy. An ion will trigger the detector when both conditions are met. The region to the right of the vertical solid line and above the dotted line represents the window of detection.

fluid changed. The C_3F_8 filled glass vessel is bombarded by a collimated bremsstrahlung beam of 4-5 MeV γ-rays from the injector of the electron accelerator at Jefferson Lab. The glass vessel is continuously scanned by a 100 Hz high-sensitivity CMOS camera mounted in a lead-shielded container.

If γ-rays from the bremsstrahlung beam interact with the fluorine via the $^{19}F(\gamma,\alpha)^{15}N$ reaction, the ^{15}N and α particles in the outgoing channel are stopped in the C_3F_8 liquid which leads to the formation of a bubble in the superheated C_3F_8. If a bubble is observed by the camera, 10 consecutive frames taken at 10 ms intervals are stored in the computer providing information about the location and the motion of the bubble in the fluid. At the same time the pressure in the bubble chamber is increased from 0.58 MPa to 2 MPa, which is above the critical pressure for C_3F_8, thus leading to a quenching of the bubble. After a recovery time of 5-10 s the pressure is again decreased to the superheated region at ~ 0.58 MPa. Details about the thermodynamics of bubble formation or the pressure control system used in the experiment can be found in [8]. The main difference between the single-fluid bubble chamber used in this experiment and the one described in [8] is the absence of a buffer fluid. In order to avoid bubble formation in the C_3F_8 region which is located outside of the field of view of the CMOS camera, the whole volume below the glass vessel containing the superheated C_3F_8 is surrounded by a separate cylindrical container kept at lower temperatures (see Fig. 2).

The required temperature can be obtained from the p-T plot for C_3F_8 shown in Fig. 1. Operating the bubble chamber at a temperature of 18°C in the pressure range from 0.58 MPa (superheated) to 2 MPa (not superheated) requires a lowering of the temperature by about 20-25°C in the area where bubble generation is to be prevented. As shown in Fig. 2 a cold region is created using a cooling circuit inside a cylindrical thermal break (labeled as pressure control in Fig. 2) which is kept below -5°C. The temperature distribution was determined with 14 RTDs mounted outside the glass vessel. Thus, at the temperature of the C_3F_8 in the lower part of the glass vessel, the bellows, and the plumbing system, the liquid never crosses the liquid-vapor phase boundary (see Fig. 1). This allows the same fluid being used as active target and as a buffer fluid.

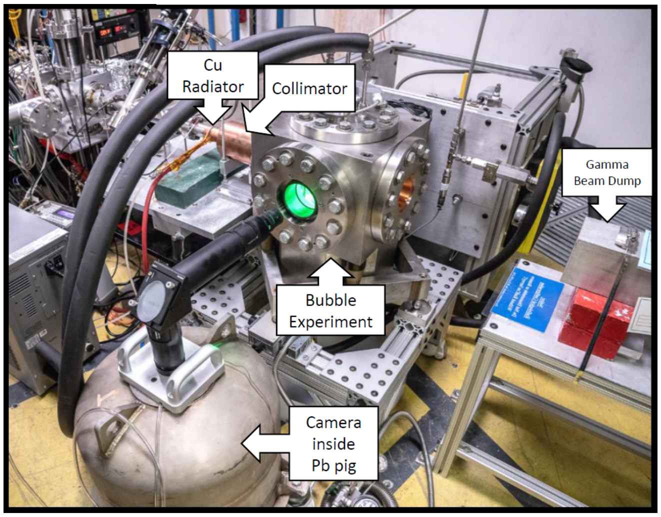

FIG. 4. The bubble experiment in the injector hall at Jefferson Lab. The electron beam comes in from the left on the 5D line. Down the beamline, the electron beam hits the copper radiator. Bremsstrahlung γ-rays produced at the radiator then go through a copper collimator. Additional collimation is provided by a tungsten insert and copper entrance flange (see Fig 2). Not shown is additional lead shielding placed around the copper radiator during experimental runs. Inside the steel pressure vessel (illuminated by the green LED) in the center of the image is the glass cell (which holds the active fluid) surrounded by a volume of mineral oil (used for thermal transfer).

TABLE I. Electron Beam Setups

Beam p (MeV/c)	Beam RMS Horiz. Size on Radiator (cm)	Beam RMS Vert. Size on Radiator (cm)	Beam K.E. (MeV)	Beam ΔE (MeV)
5.299	0.170	0.057	4.803	0.010
5.406	0.087	0.122	4.910	0.010
5.517	0.151	0.280	5.020	0.008
5.605	0.041	0.126	5.109	0.007
5.703	0.102	0.118	5.208	0.008
5.840	0.051	0.053	5.341	0.010
5.887	0.162	0.048	5.393	0.012

III. γ-RAY BEAM PRODUCTION

The bremsstrahlung γ-ray beam was produced by impinging an electron beam accelerated by Jefferson Lab's injector on a copper radiator. The injector has a photocathode source operating at 130 kV with GaAs [27] as the photo-cathode material to provide polarized electron beams to nuclear physics experiments in Jefferson Lab's experimental halls. After bunching at 130 keV, the beam is accelerated to 500 keV with a low Q graded β 5-cell radiofrequency (RF) cavity before being accelerated to relativistic energies (or nearly relativistic energies as required) in 2 5-cell superconducting RF cavities known as the quarter cryomodule. Downstream of the quarter cryomodule is a transport section with four beamlines served by a common dipole: a straight ahead line (0L) to deliver beam to the next stage of acceleration before the beam is merged into the main CEBAF accelerator and three spectrometer dump lines (2D, 3D, and 5D). The 2D and 5D dump lines form -30° and 25° angles, respectively, with the straight ahead 0L line. The bubble chamber was installed on the 5D line. Setting and measuring the electron beam characteristics for the experiment used the 0L, 5D, and 2D lines.

Throughout the experiment, the cavities in the quarter cryomodule were operated on-crest providing maximum energy gain from each cavity, and the gradient setpoints of the two cavities were adjusted to set the momentum of the beam to match the calculated spectrometer dipole setting for the desired beam momentum in the 5D line. Beam position monitor (BPM) readbacks in the 5D line determined when the momentum matched the dipole setting. The momentum was measured using both the 2D and 5D lines under the assumptions that the momentum of the beam coming into the spectrometer dipole is fixed and proportional to the angle (and therefore dipole setting) required to bend the beam into the respective dump line. The beam momenta measured using this method and associated errors are summarized in Tables III and IV.

In addition to transport optics, the 0L line is instrumented with BPMs and a wire scanner for measuring the beam centroid and size. The 2D line has a wire scanner and BPM, and the 5D line has transport optics, BPMs, and a wire scanner upstream of the radiator. Using an `elegant` [28] model for the optics in the individual lines and measurements from the wire scanners, simulations provide the momentum or energy spread of the beam (Table V) and the beam size at the radiator (Tables VI and VII).

With a beamline model of the 5D beamline elements between the spectrometer dipole and the radiator (3 corrector pairs, 2 quadrupoles, and 2 BPMs) including the background earth's field, General Particle Tracer (`gpt`) [29] simulations provide estimates of the position and angle of the beam on the radiator in Table VIII. The simulations used the measured beam positions from the BPMs and the control system setpoints for the corrector and quadrupole magnets to determine the likely beam orbit at the radiator.

IV. DETECTION EFFICIENCIES AND BACKGROUND MEASUREMENTS

The response of the single-fluid bubble chamber to incoming neutrons was tested by exposing the detector to neutrons from Pu-^{13}C and Am-Be sources located at distances between 0.9 m and 7 m. The detection efficiency was found to be constant in the cylindrical section of the glass vessel as shown in Fig. 7.

Since the production efficiency for bubbles depends also on the amount of superheat in the detector [30] the data presented below have been corrected for changes in

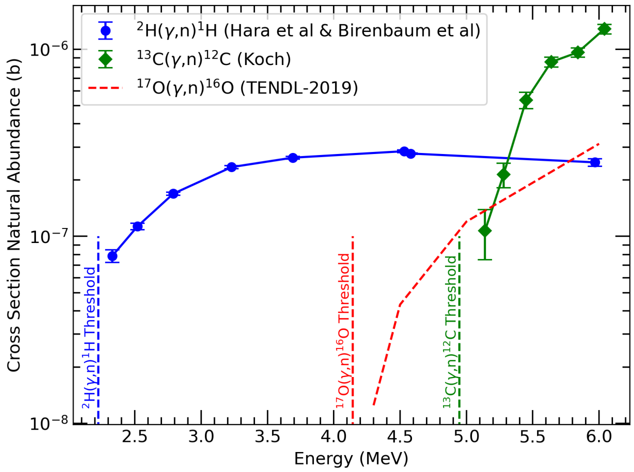

FIG. 5. (Color online) Cross sections of the three $(\gamma$,n) reactions, multiplied by the abundance of each isotope, which can contribute to the beam induced background of the experiment. The threshold of each reaction are denoted by the vertical dashed lines. Over the energy ranges of this experiment, the neutron background predominately comes from ^{2}H$(\gamma$,n) with ^{13}C$(\gamma$,n) becoming important at higher energies. See text for details.

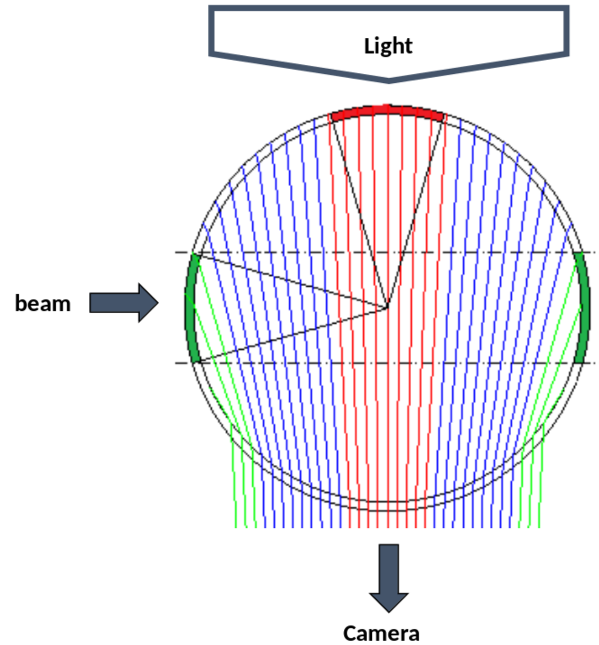

FIG. 6. (Color online) Effect of refraction on the location of the bubbles from background events at the glass surface occurring in an angular region covering a range of 30°. Background events from the ^{10}B(n,α)^{7}Li reaction originate at two regions (green) along and perpendicular to the incoming beam. Colors guide the eye through various light trajectories.

pressure and temperature which occurred during the experiment. These corrections are typically of the order of < 25 %. For measurements of the yield at a given energy a weighted average of the number of bubbles in the fiducial minus the background area was calculated.

There are several possible sources of background events in this experiment. Since bubble chambers are insensitive to γ-radiation there are no contributions from γ-ray emitting contaminants such as ^{40}K. To eliminate contributions from α-emitting isotopes (e.g. Ra, Th, U) which can be present in minute amounts in the material used for the construction of the detector, cleaning procedures as described in Dark Matter experiments have been employed [31], which give typical event rates from the walls of the glass vessel of 4 events/day.

A second source of background originates from cosmic rays that are detected in the bubble chamber. The flux of secondary cosmic-ray neutrons at sea level is typically ~ 0.01 neutrons/cm^2/sec [32]. At the location of the experiment which is ~ 10 m.w.e. underground this rate is $\sim 10^{-4}$ neutrons/cm^2/sec. Muons, which are, after neutrons the second most abundant particles in the cosmic rays, do not lead to bubble formation under the operating conditions of the bubble chamber used in this experiment. However, cosmic ray muons can create neutrons via spallation on nuclei. The cosmic background rate has been measured over a period of 76 hrs during the experiment and was found to be about 8×10^{-3} events/sec, in good agreement with the expected flux from cosmic ray induced neutrons. A spectrum of these events taken over a period of 2 hours is shown in panel b) of Fig. 7.

A general feature of the bubble distributions shown in the four panels of Fig. 7 is an increase in the number of bubbles at the interface between the glass and the superheated fluid. This increase is caused by the presence of boron oxide (typically 15 - 20%) in silicate glasses which is added to increase their chemical durability. Incoming low-energy neutrons from the AmBe source, from cosmic rays or from $(\gamma$,n) neutrons produced in the material surrounding the bubble chamber can interact with the ^{10}B in the glass via the ^{10}B(n,α)^{7}Li producing ^{4}He and ^{7}Li nuclei with energies between 1-2 MeV, which is sufficient to generate a bubble in the superheated fluid.

The spatial distribution of these bubbles is further influenced by refractive effects. Fig. 6 shows a simulation of the refraction effects observed in the bubble chamber consisting of a glass tube (n=1.47) filled with liquid C_3F_8 (n=1.22) and surrounded by the hydraulic fluid (n=1.45) [33]. In the experiment the glass tube is illuminated from the side and viewed at the opposite end by the CCD camera (see Fig. 4). As can be seen from the calculation a section of the glass surface located perpendicular to the viewing direction is compressed by a factor of 2 when compared to the same area located along the viewing direction, leading to a concentration of the bubbles on the left and right side of the glass vessel. This effect is even more pronounced in the dome-like structure at the top of the glass vessel. Details will be given in a separate paper [34]. For this reason, the size of the fiducial area in the beam direction has been reduced as shown in Fig. 7 and

Fig. 8 and the detection efficiency has been corrected accordingly.

Candidates for the production of (γ, n) neutrons from the bremsstrahlung beam interacting with materials surrounding the bubble chamber involve isotopes where the neutron separation energy is lower than the energy of the incident γ-rays (e.g. ^{2}H, ^{13}C and ^{17}O). If the energy of these neutrons is above 0.5 MeV they can elastically scatter on the superheated C_3F_8 with the recoiling C and F nuclei producing bubble events. As mentioned in the previous paragraph, lower energy neutrons cab also be produce charged particles through the ^{10}B(n,α)^{7}Li reaction which are found to be the main source of the background events. The four primary beam-induced background reactions are summarized below.

a) ^{2}H(γ,n)^{1}H (threshold = 2.224 MeV, abundance = $1.15{\times}10^{-4}$). Deuterium is present in the mineral oil surrounding the glass cell. Because of its low Q value, the resulting neutrons have sufficient kinetic energy to create bubbles by elastically scattering off the C and F nuclei in the active fluid. Because of its low threshold neutrons from this reaction are present at all energies where measurements were taken.

b) ^{13}C(γ,n)^{12}C (threshold = 4.946 MeV, abundance = $1.07{\times}10^{-2}$). ^{13}C is present in the mineral oil and in the active fluid C_3F_8. Due to its high reaction threshold, it is only relevant at the highest beam energies. The larger Q value means that most neutrons from this reaction do not have enough kinetic energy to create bubbles by elastic scattering in the active fluid. However, at the highest energies this reaction yields around an order of magnitude higher neutron flux compared to ^{2}H(γ,n)^{1}H.

c) ^{17}O(γ,n)^{16}O (threshold = 4.143 MeV, abundance = $3.8{\times}10^{-4}$). Oxygen is present in the glass and the oil surrounding the superheated fluid. The higher threshold compared to deuterium yields neutrons with insufficient energies to create bubbles via elastic scattering, but oxygen is a very abundant element in the bubble chamber.

d) ^{10}B(n,α)^{7}Li (threshold = 0.0 MeV, abundance = 0.199). ^{10}B is present in the borosilicate glass. The (n, α) reaction occurring at the C_3F_8-glass interface is the possible source of surface events discussed above.

A. Effects of beam-induced background

The cross sections for the (γ, n) reactions on ^{2}H [35, 36], ^{13}C [37] and ^{17}O (interpolated TENDL data) [38] multiplied by the natural abundance are shown in Fig. 5. From these three reactions only ^{2}H(γ,n)p (Q=-2.22 MeV) and ^{17}O(γ,n)^{16}O (Q=-4.142 MeV) have low enough Q-values in order to produce neutrons in the full energy range covered in this experiment. As shown in Fig. 2, oxygen and hydrogen are present in the beam path of the γ-rays in the walls of the glass vessel and in the hydraulic fluid surrounding the bubble chamber. While the two isotopes ^{17}O and ^{2}H have natural abundances of only 1 - $3{\times}10^{-4}$, they can still dominate the background events. (See Fig. 7 above.) From the (γ,n) cross sections in Fig. 5 one can see that in the energy region $E_\gamma < 5$ MeV deuterium is the main source of background events, while for higher energies ^{17}O (and later ^{13}C) contribute as well. This background can be eliminated in the future by switching to a fluorine containing hydraulic fluid.

The distribution of bubbles, from the 30 mCi AmBe source (Fig. 7a) shows bubbles created uniformly over the active fluid. The neutrons from this source, having a mean energy of 4 MeV, are able to create bubbles by elastically scattering off carbon and fluorine nuclei in the active fluid. A similar distribution is seen in the data from the cosmic rays (second from the left). In both the AmBe and cosmic ray data the surface events, which can be seen in the c) and d) of Fig. 7 where the electron beam is on, are not present. This is explained by the relative flux of neutrons from the different sources. In the AmBe and cosmic ray case, the neutron flux is small while the average neutron energy is quite high. Contrarily, neutrons produced via the (γ,n) reactions in the mineral oil are much higher in flux but the mean energy is considerably lower. Since the cross section for ^{10}B(n,α)^{7}Li increases as the neutron energy gets smaller, the rate of wall events from the resulting lithium nuclei is considerably larger when the beam is on compared to the rate of wall events produced by high-energy neutrons from the AmBe source or from cosmic rays.

V. EXPERIMENTAL RESULTS

An excitation function for the photodisintegration reaction ^{19}F$(\gamma, \alpha)^{15}$N was measured in the energy range from 4.0 MeV to 5.4 MeV. The location of the bubbles in the 10 consecutive pictures mentioned in sec. II were analyzed with a software package which allowed to select bubbles with similar radii and velocities. Details of this analysis will be published in a separate paper [34].

A. Distribution of bubbles

The location of bubble events taken at four energies with electron currents covering the range from 6 nA to 45 μA is shown in Fig. 8. At the highest energies the data overlaps with the previous experiment performed at the HIγS facility and extends to 4.0 MeV which is below the ^{19}F$(\gamma, \alpha)^{15}$N threshold located at 4.014 MeV. The cross sections calculated from the known resonance parameters and branching ratios cover the range from 6 μb to $\sim$40 pb. These cross sections have to then be folded with the energy distribution of the bremsstrahlung

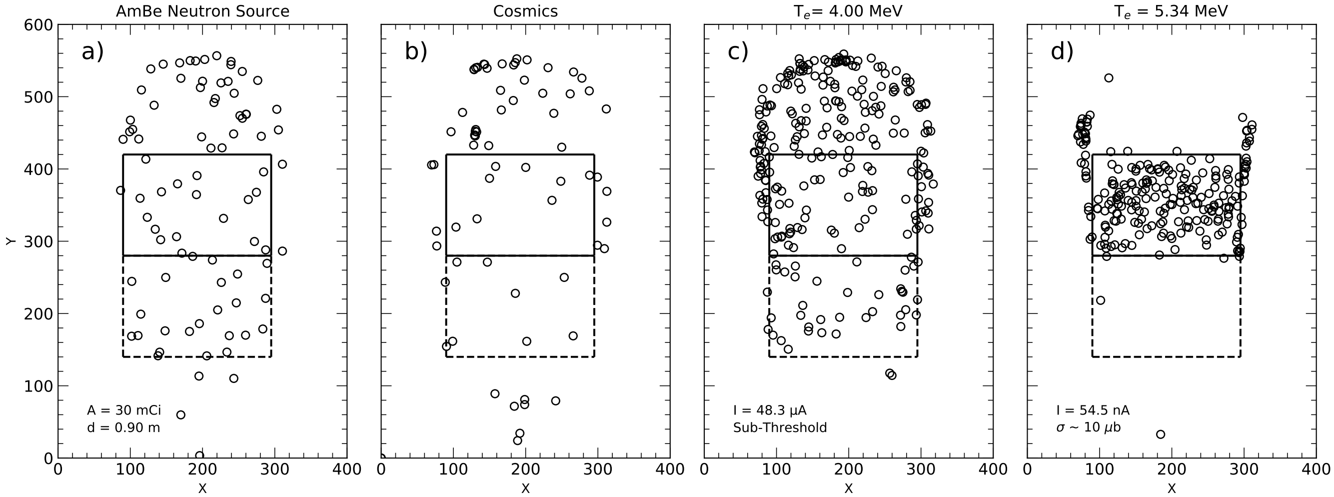

FIG. 7. Bubble distributions resulting from AmBe neutron source (a), from cosmic rays (b), and bremsstrahlung beam produced from an electron beam with energies of 4.0 MeV (c), and 5.34 MeV (d). See text for details.

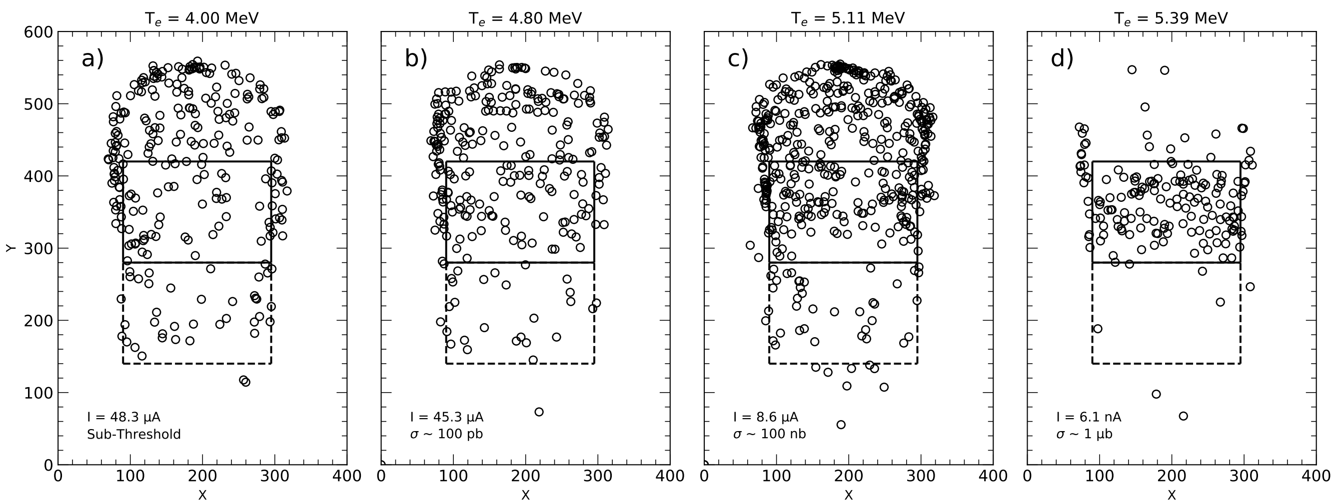

FIG. 8. Distribution of events measured in the bubble chamber at various bombarding energies using a bremsstrahlung beam produced from an electron beam with energies of T_e. The electron currents (I) as well as the estimated cross sections of the $^{15}N(\alpha,\gamma)^{19}F$ at these energies are included. (see text for details). At the highest energy point (d) the bubbles resulting from the γ-ray beam form a defined fiducial region (solid black line). This region is used for all energies. Below this fiducial region an equally sized "background" region (dashed black line) is used for background subtraction.

beam which will be discussed in Section V D. Since the bremsstrahlung beam passes through a 15.24 cm long Cu collimator (inner diameter of 8 mm) photodissociation events in the C_3F_8 fluid have to be located in a cylinder-shaped fiducial area which is shown by the solid lines in Fig. 8. Events on the right and left side of the fiducial area are caused by background events in the wall of the glass vessel (e.g. from the $^{10}B(n,\alpha)^7Li$ reaction) ([39]) which, through refraction effects, are concentrated in vertical regions on the right and left of the fiducial area [34]. In order to subtract events from cosmic rays a background area was defined below the fiducial area as shown by the dot-dashed line in Fig. 8.

B. Experimental Yield

$$Y = \frac{F - B}{I(t_{tot} - \tau N_{tot})} \tag{1}$$

For each of the experimental runs a yield is defined by

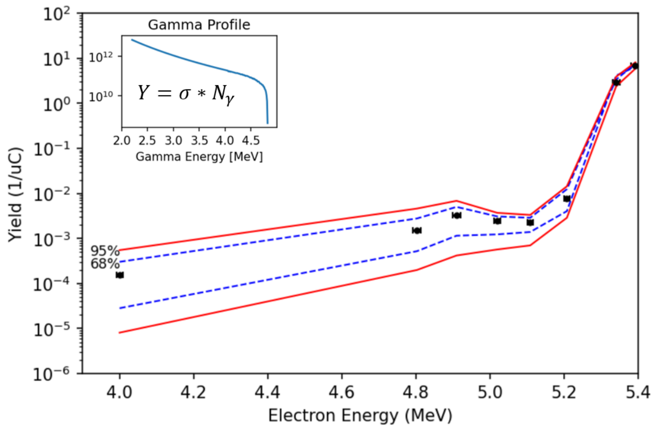

FIG. 9. (Color online) Experimental yields defined by the equation (F-B)/I where F and B are the counts in the fiducial and background regions shown by the solid and dot-dashed lines in Fig. 8. I is the dead-time corrected electron beam current (in μA) used for the production of the bremsstrahlung beam.

eq. 1 where F and B are the number of bubbles observed in the fiducial and background areas, respectively, N_{tot} is the total number of bubbles, t_{tot} the total runtime, τ the deadtime (10 sec) and I is the incident electron current (in μA). The yield then amounts to the number of bubbles per dead-time corrected electron beam charge. The range in yield covered in this experiment extends over more than four orders of magnitude.

For each energy, a weighted average yield is computed which gives the central values (black dots) in Fig. 9. Where the statistical weight of each run, within a given energy, is set by the quantity F - B. To determine confidence intervals a simple Monte-Carlo calculation samples over the parameters of Eq. 1. The beam current for each run is recorded from two beam-line ammeters (detailed in sec. III), from which the average beam current with Gaussian error bars for each run is determined. For F, B and N_{tot} error bars are assumed from simple counting errors. From the MC sampling the Gaussian 68% and 95% confidence intervals are computed, as shown by the dotted blue line and solid red line, respectively, in Fig. 9.

C. GEANT4 Simulations

From the measured electron beam parameters, the resulting bremsstrahlung beam is determined using GEANT4 [40–42]. The engineering CAD files of the components were imported into the simulation. Surveys taken at Jefferson Lab recorded the position of the copper radiator, pressure vessel, and Al beam dump relative to the 5U dipole. From this survey the components in the simulation are aligned to match the experimental conditions.

The choice of physics list for the simulation is dictated by the need for an accurate simulation of the production of the bremsstahlung beam off the copper radiator, and the transport of the γ-rays through to the glass cell. For electromagnetic physics the GEANT4 Livermore E&M library (EM Liv) was used. This uses the Seltzer-Berger model [43] at the energy range of this experiment. For hadronic physics three models were tested, a Bertini cascade model [44, 45], a Bertini cascasde with high precision neutron data [46] (ENDF/B-VIII.0), and Binary cascade model [47]. Since the complete characterization of the backgrounds using GEANT4 was outside the scope of this work (but will be performed in a future work), simulation was focused on producing a high quality gamma ray spectrum inside the glass cell and thus little changes were seen across the three different hadronic physics list. The Bertini cascade model without high precision neutron data was selected for the final production simulations as it performed slightly faster.

To check the physics and geometry of our GEANT4 model, simple simulations were performed to model the AmBe neutron source tests. With the number of neutrons and their energy spectrum recorded for simulations of the source at the same three distances tested with the bubble experiment at the Jefferson Lab injector hall. From these neutron spectra the estimated number of bubbles in the active fluid was found to be in good agreement with the experimental results at the two largest distances, with the result with the source closest to the bubble experiment being within the 2-σ error bars of the experimental result.

GEANT4 simulations were preformed at each of the principal energies listed in Table I in addition to a simulation using a beam with an electron kinetic energy of 4.0 MeV. For each of these energies 10^{11} electrons were simulated using the Jefferson Lab experimental physics compute farm. The primary sensitive volume was the glass cell (which houses the active fluid). An additional sensitive volume was placed directly after the Cu radiator to measure the γ-ray flux in the forward direction. This allows for a double check of the simulation (electrons with a Gaussian energy spread hitting a Cu radiator is a well known problem) and to check how well the Cu collimator and W-alloy insert produce a defined γ-ray cone in the active fluid. In both sensitive volumes, the number of γ-rays entering the volume, their kinetic energy, and their 2D position on a plane perpendicular to the primary beam axis were recorded. From this, the bremsstrahlung profile and the γ-ray beam shape in the active fluid was constructed. Integrating over the 2D γ-ray distribution inside the glass cell a circular area containing approximately 95% of the γ-rays was found to have a diameter closely matching the size of the fiducial region described in sec. V A (diameter consistent with the height of the solid box in Fig. 7 and 8). The ratio of the number of simulated electrons to the number of γ-rays reaching the glass cell was then used to scale up the simulation to match the total beam current at each of the eight beam energies (values in Table I plus 4.0 MeV).

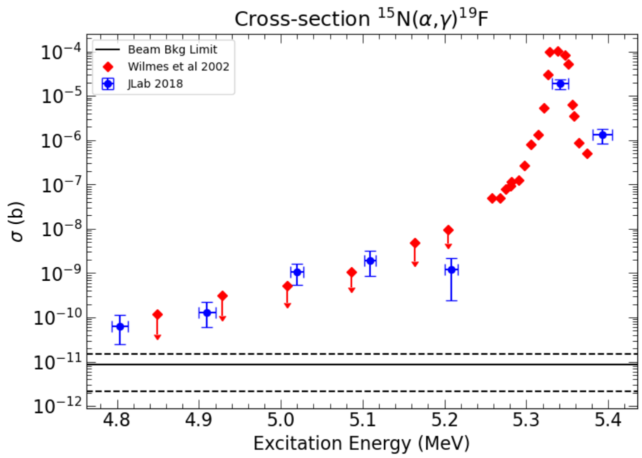

FIG. 10. (Color online) Comparison of experimental cross sections from Wilmes et al [13] in red and JLab 2018 (this work) in blue. The solid black horizontal line is the beam background limit of the current bubble chamber setup. The dashed black horizontal lines represent the 1σ limits on the beam background.

D. Determining Cross Section

The experimental yield shown in Fig. 9 can be recast using the simulated γ-ray spectrum detailed in the previous section. This provides a relationship between the number of bubbles estimated to come from the $^{19}F(\gamma,\alpha)^{15}N$ resulting from the number of γ-rays used at a given energy point. The relationship between the cross section and experimental yield is given by a simple convolution

$$Y = \sigma * N_\gamma \tag{2}$$

with Y the experimental yield (as calculated in Eq. 1) and N_γ the bremsstrahlung spectrum.

To obtain the cross section one can solve this in the "backwards direction" (deconvoluting the experimental yield with the bremsstrahlung profiles to get the cross section) or in the"forward direction" (convolute the bremsstrahlung profiles using a known or modeled cross section). In general, convolution is much simpler than deconvolution. A method to perform this deconvolution with the assistance of machine-learning methods will be explored in a future work. For this current work, the bremsstrahlung profiles described in sec. V C was convoluted with the Breit-Wigner cross section of the $^{19}F(\gamma,\alpha)^{15}N$ reaction. From this theoretical yield we then compare to the experimentally measured yield and then determine the corresponding experimental values of the cross section. The results of this are shown as the blue circular dots in Fig. 10. From the sub-threshold measurement at 4.0 MeV we determined the beam background limit of the current bubble chamber setup shown as the solid black horizontal line in Fig. 10.

VI. SUMMARY AND FUTURE PLANS

Compared to our earlier experiment described in Ref.[7] the cross section limits of $^{15}N(\alpha,\gamma)^{19}F$ reaction have been pushed down by about two orders of magnitude reaching cross sections of $\sim$60 pb, thus, measuring values in an energy region where so far only upper limits of $\sim$120 pb have been obtained. Although we are not yet in the single picobarn range further improvements of this technique are possible. Due to the high luminosity of this technique achieved through the use of thick targets ($\sim$10 g/cm^2) and a higher phase-space factor the present limits of the cross sections are caused mainly by background events from reactions in the wall of the glass vessel. These events can be further reduced by improved neutron shielding, by eliminating the ^{10}B content in the glass (through the use of pure Si-quartz glass) and by replacing the hydraulic oil with hydrogen-free fluid. We have also designed a compact stereo camera that will allow us to determine the 3D location of the bubble even under the space restrictions of the existing pressure vessel. With these improvements cross section measurements of (α,γ) reactions with cross sections in the pb range should become accessible.

In the future, we could study helium-induced nuclear reactions, which are of importance in many astrophysical scenarios. Also, Big Bang produces primordial lithium with an abundance that shows a discrepancy between observations and model predictions, which is known as the lithium problem [48]. While it is unlikely that the solution is of nuclear origin, one possibility involves the production of lithium through the ^{3}He(^{4}He, γ)^{7}Be(β^+)^{7}Li process, but the radiative capture of α particles on deuterium and tritium are two other possible nucleosynthetic paths to generate lithium. A bubble chamber containing a lithium compound dissolved in liquid ammonia is under consideration.

A bubble chamber with a liquid containing a magnesium solution could also be used to study the photodisintegration of ^{26}Mg to determine the rate of the $^{22}Ne(\alpha,\gamma)^{26}Mg$ neutron poison reaction [49]. The weak component of the s process is responsible for the production of nuclei with 60$\leq$A$\leq$90 in massive stars. It requires a neutron density of $\sim1\times10^{12}$ cm^{-3}, which is provided mainly by the $^{22}Ne(\alpha,n)^{25}Mg$ reaction. The number of neutrons produced depends not only on the cross section but also on the rate of the $^{22}Ne(\alpha,\gamma)^{26}Mg$ reaction –an alternate competing process that "poisons" the production of neutrons. Both rates are uncertain at temperatures relevant to the weak component of the s process.

The $^{12}C(\alpha,\gamma)^{16}O$ reaction has been studied in normal and inverse kinematics for more that 50 years and cross section limits in the $\sim$pb range have been obtained [2]. For measurements of the photodissociation reaction $^{16}O(\gamma,\alpha)^{12}C$ using a bubble chamber oxygen-containing superheated liquids of H_2O, CO_2 and N_2O have been tested so far [34]. The main difficulty for this reaction originates from the competing $^{17}O(\gamma,\alpha)^{13}C$ and

TABLE II. Experiment Summary Table - Sum Over All Runs At Given Electron Beam Energy

Electron Beam K.E. (MeV)	**Total Charge (μC)**	**Total Active Runtime (s)**	**$N_\gamma(T_\gamma \geq 4.0)$ from GEANT4**	**N_{tot}**	**Est. $N_{Cosmics}$**	**F - B**
4.0	1.44×10^5	3 042	-	328	25	17
4.803	4.71×10^5	21 093	5.96×10^{12}	3 472	171	419
4.910	7.55×10^5	15 964	4.97×10^{12}	2 316	130	279
5.020	9.51×10^4	13 461	2.10×10^{12}	1 715	109	211
5.109	1.84×10^5	7 811	4.58×10^{12}	1 032	63	207
5.208	3.98×10^4	29 400	1.27×10^{12}	1 440	239	269
5.341	1.68×10^2	6 671	6.94×10^9	478	54	310
5.393	3.79×10^1	7 175	1.54×10^9	397	58	246

^{18}O(γ,α)^{14}C reactions with Q-values of -6.357 MeV and -6.227 MeV, respectively, which are smaller than the one for photodissociation of ^{16}O (Q=-7.162 MeV). Thus, this measurement requires the use of highly-enriched oxygen, in order to eliminate the contributions from the ^{17,18}O isotopes. Measurements of these background reactions are planned in the near future.

VII. ACKNOWLEDGEMENTS

The authors would like to thank the accelerator staff at the Thomas Jefferson National Accelerator Facility for their support. We would also like to thank Maurizio Ungaro for his help with the GEANT4 simulations. This work was supported by the US Department of Energy, Office of Nuclear Physics, under Contract No. DE-AC02-06CH11357 and DE-AC05-06OR23177.

[1] D. Trezzi *et al.*, Astropart. Phys. **89**, 57 (2017).
[2] R. J. deBoer *et al.*, Rev. Mod. Phys. **89**, 035007 (2017).
[3] D. Schürmann, L. Gialanella, R. Kunz, and F. Strieder, Phys. Lett. B **711**, 35 (2012).
[4] K. Fujita *et al.*, Few-Body Syst. **54**, 1603 (2013).
[5] need ref. from Claudio, need ref. from Claudio.
[6] G. Baur, C. Bertulani, and H. Rebel, Nucl. Phys. A **458**, 188 (1986).
[7] C. Ugalde *et al.*, Phys. Lett. B **719**, 10.1016/j.physletb.2012.12.068 (2013).
[8] B. DiGiovine *et al.*, Nucl. Instrum. Meth. A **781**, 96 (2015).
[9] V. Zacek, Il Nuovo Cimento A (1965-1970) **107**, 291 (1994).
[10] W. Bolte *et al.*, Nucl. Instrum. Meth. A **577**, 569 (2007).
[11] E. Ramberg *et al.*, Nucl. Instrum. Meth. A **623**, 454 (2010).
[12] S. Wilmes *et al.*, Phys. Rev. C **52**, R2823 (1995).
[13] S. Wilmes *et al.*, Phys. Rev. C **66**, 065802 (2002).
[14] A. Di Leva *et al.* (ERNA Collaboration), Phys. Rev. C **95**, 045803 (2017).
[15] H. R. Weller *et al.*, Prog. Part. Nucl. Phys. **62**, 257 (2009).
[16] D. A. Glaser, Phys. Rev. **91**, 762 (1953).
[17] M. Barnabe-Heider *et al.*, Nucl. Instrum. Meth. A **555**, 184 (2005).
[18] E. Behnke *et al.* (COUPP Collaboration), Phys. Rev. D **86**, 052001 (2012).
[19] M. Felizardo *et al.* (The SIMPLE Collaboration), Phys. Rev. Lett. **105**, 211301 (2010).
[20] C. Amole *et al.* (PICO Collaboration), Phys. Rev. Lett. **114**, 231302 (2015).
[21] J. R. Waters, C. Petroff, and W. S. Koski, IEEE T. Nucl. Sci. **16**, 398 (1969).
[22] C. Dodd, P. Phys. Soc. Lond. B **68**, 686 (1955).
[23] G. Brautti, M. Ceschia, and P. Bassi, Il Nuovo Cimento (1955-1965) **10**, 1148 (1958).
[24] CERN, Detector cooling section - c3f8 properties, `https://detector-cooling.web.cern.ch/fluidmaterial.html#fluid` (2022).
[25] F. Seitz, Phys. Fluids **1**, 2 (1958).
[26] M. J. Harper, Nucl. Sci. Eng. **114**, 118 (1993).
[27] P. Adderley *et al.*, Phys. Rev. ST: Accel. Beams **13**, 010101 (2010).
[28] M. Borland, in *6th International Computational Accelerator Physics Conference (ICAP 2000)* (2000).
[29] S. van der Geer and M. de Loos, General particle tracer, `http://www.pulsar.nl.gpt` (2018).
[30] F. Poesposoetjipto and E. Hugentobler, Helv. Phys. Acta **43** (1970).
[31] Cleaning procedure.
[32] J. F. Ziegler *et al.*, IBM J. Res. Dev. **40**, 51–72 (1996).
[33] M. L. Lowe and P. H. Kutt, Exp. Fluids **13**, 315 (1992).
[34] B. DiGiovine *et al.*, to be published.
[35] K. Y. Hara *et al.*, Phys. Rev. D **68**, 072001 (2003).
[36] Y. Birenbaum, S. Kahane, and R. Moreh, Phys. Rev. C **32**, 1825 (1985).
[37] R. Koch and H. Thies, Nucl. Phys. A **272**, 296 (1976).
[38] A. Koning, D. Rochman, J.-C. Sublet, N. Dzysiuk, M. Fleming, and S. van der Marck, Nucl. Data Sheets **155**, 1 (2019), special Issue on Nuclear Reaction Data.
[39] wall events.
[40] S. Agostinelli *et al.*, Nucl. Instrum. Meth. A **506**, 250 (2003).
[41] J. Allison *et al.*, IEEE T. Nucl. Sci. **53**, 270 (2006).

TABLE III. Beam Momenta

Design p (MeV/c)	2D line dipole setting (G cm)	5D line dipole setting (G cm)	Measured p (MeV/c)	Measured K.E. (MeV)
5.24	-8958	7339	5.299	4.803
5.34	-9136	7490	5.406	4.910
5.44	-9321	7647	5.517	5.020
5.54	-9469	7771	5.605	5.109
5.64	-9632	7909	5.703	5.208
5.74	-9866	8099	5.840	5.341
5.84	-9938	8169	5.887	5.393

[42] J. Allison *et al.*, Nucl. Instrum. Meth. A **835**, 186 (2016).
[43] S. M. Seltzer and M. J. Berger, Nuc. Inst. Meth. Phys. B **12**, 95 (1985).
[44] M. Guthrie, R. Alsmiller, and H. Bertini, Nucl. Instrum. Methods **66**, 29 (1968).
[45] A. Heikkinen, N. Stepanov, and J. P. Wellisch, eConf **C0303241**, MOMT008 (2003), arXiv:nucl-th/0306008.
[46] E. Mendoza, D. Cano-Ott, T. Koi, and C. Guerrero, IEEE T. Nucl. Sci. **61**, 2357 (2014).
[47] G. Folger, V. N. Ivanchenko, and J. P. Wellisch, Euro. Phys. J. A **21**, 407 (2004).
[48] B. D. Fields, Annu. Rev. Nucl. Part. Sci. **61**, 47 (2011).
[49] F. Herwig, Annu. Rev. Astron. Astrophys. **43**, 435 (2005).

Appendix: Determination of electron beam parameters

The Jefferson Lab's injector has a photo-cathode source operating at 130 kV with GaAs [27] as the photo-cathode material to provide polarized electron beams to nuclear physics experiments in Jefferson Lab's experimental halls. After bunching at 130 keV, the beam is accelerated to 500 keV with a low Q graded β 5-cell radiofrequency (RF) cavity before being accelerated to relativistic energies (or nearly relativistic energies as required) in 2 5-cell superconducting RF cavities known as the quarter cryomodule. Downstream of the quarter cryomodule is a transport section with four beamlines served by a common dipole: a straight ahead line (0L) to deliver beam to the next stage of acceleration before the beam is merged into the main CEBAF accelerator and three spectrometer dump lines (2D, 3D, and 5D). The 2D and 5D dump lines form -30° and 25° angles, respectively, with the straight ahead 0L line. The bubble chamber was installed on the 5D line. Setting and measuring the electron beam characteristics for the experiment used the 0L, 5D, and 2D lines.

Throughout the experiment, the cavities in the quarter cryomodule were operated on-crest providing maximum energy gain from each cavity, and the gradient setpoints of the two cavities were adjusted to set the momentum of the beam to match the calculated spectrometer dipole setting for the desired beam momentum in the 5D line.

TABLE IV. Beam Momenta Errors

Contribution	Value (%)
Power Supply Calibration (2 mA)	0.06
Power Supply Regulation (1.5 mA)	0.04
Spectrometer dipole field map offset (7 G-cm)	0.08
Spectrometer dipole model	0.10
Tracking model (0.006 MeV/c)	0.11
Total	0.18

TABLE V. Momentum or Energy spread (dp/p)

Measured p (MeV/c)	dp/p ($\times10^{-3}$)	Measured p (MeV/c)	dp/p ($\times10^{-3}$)
5.299	1.76	5.703	1.28
5.406	1.72	5.840	1.50
5.517	1.27	5.887	1.88
5.605	1.17		

Beam position monitor (BPM) readbacks in the 5D line determined when the momentum matched the dipole setting. The momentum was measured using both the 2D and 5D lines under the assumptions that the momentum of the beam coming into the spectrometer dipole is fixed and proportional to the angle (and therefore dipole setting) required to bend the beam into the respective dump line. The beam momenta measured using this method and associated errors are summarized in Tables III and IV.

In addition to transport optics, the 0L line is instrumented with BPMs and a wire scanner for measuring the beam centroid and size. The 2D line has a wire scanner and BPM, and the 5D line has transport optics, BPMs, and a wire scanner upstream of the radiator. Using an `elegant` [28] model for the optics in the individual lines and measurements from the wire scanners, simulations provide the momentum or energy spread of the beam (Table V) and the beam size at the radiator (Tables VI and VII).

With a beamline model of the 5D beamline elements between the spectrometer dipole and the radiator (3 corrector pairs, 2 quadrupoles, and 2 BPMs) including the background earth's field, General Particle Tracer (`gpt`) [29] simulations provide estimates of the position and angle of the beam on the radiator in Table VIII. The simulations used the measured beam positions from the BPMs and the control system setpoints for the corrector and quadrupole magnets to determine the likely beam orbit at the radiator.

TABLE VI. Horizontal beam size at wire scanner and extrapolated beam size at the radiator

Measured p (MeV/c)	Wire Scanner RMS size (mm)	RMS size (mm)	Note
5.299	1.312	1.698	05142018 22:35:00 measurement prior to data taking is different from 05162018 13:21:51 re-measurement after data taking (latter reported)
5.406	0.7528	0.8670	05132018 22:39:02
5.517	0.4907	0.3093	05162018 19:01:44
5.517	1.11	1.51	05172018 11:28:02 (larger spot size)
5.605	0.1532	0.4092	05122018 16:11:48
5.703	0.6809	0.6575	05152018 23:29:41 poor beam position on radiator
5.703	0.9079	1.023	05162018 09:45:50 centered on radiator
5.840	0.7493	0.7416	05112018 22:04:10
5.840	0.5721	0.5100	05132018 15:34:03
5.887	1.342	1.623	05172018 23:59:19

TABLE VII. Vertical beam size at wire scanner and extrapolated beam size at the radiator

Measured p (MeV/c)	Wire Scanner RMS size (mm)	RMS size (mm)	Note
5.299	0.6964	0.5736	05142018 22:35:00 measurement prior to data taking is different from 05162018 13:21:51 re-measurement after data taking (latter reported)
5.406	0.9905	1.224	05132018 22:39:02
5.517	1.001	1.220	05162018 19:01:44
5.517	2.296	2.793	05172018 11:28:02 (larger spot size)
5.605	1.013	1.261	05122018 16:11:48
5.703	0.9945	1.190	05152018 23:29:41 poor beam position on radiator
5.703	1.137	1.180	05162018 09:45:50 centered on radiator
5.840	0.5956	0.7936	05112018 22:04:10
5.840	0.4482	0.5249	05132018 15:34:03
5.887	0.405	0.4781	05172018 23:59:19

TABLE VIII. Beam Positions and Angles at the radiator (RHCS) listed in the same order as Tables VI and VII

Measured p (MeV/c)	**Horizontal angle (mrad)**	**Horizontal position (mm)**	**Vertical angle (mrad)**	**Vertical position (mm)**
5.299	-0.64	2.26	-1.06	-1.15
5.406	-1.90	0.99	-3.42	-5.24
5.517	-1.61	-0.26	0.00	0.66
5.517	-1.63	-0.29	-0.38	0.10
5.605	-3.67	-0.78	-1.17	-1.17
5.703	-3.73	-2.36	0.20	1.03
5.703	-2.36	0.45	-0.39	0.23
5.840	-2.60	0.32	-0.96	-0.91
5.840	-2.30	1.02	-0.66	-0.46
5.887	-3.58	0.95	4.02	0.86